Journal of
Marine Science and Technology

Volume 31 | Issue 1 Article 2

Application of Unmanned Aerial Vehicle–Based Infrared Images in Determining Characteristics of Sea Surface Temperature Distribution

Hsing-Yu Wang
Assistant Professor, Department of Shipping Technology, College of Maritime, National Kaohsiung University of Science and Technology

Hui-Ming Fang
Assistant Professor, Bachelor Degree Program in Ocean Engineering and Technology, National Taiwan Ocean University

Yun-Chih Chiang
Associate Professor, Center for General Education, Tzu Chi University, ycchiang@gms.tcu.edu.tw

Recommended Citation
Wang, Hsing-Yu; Fang, Hui-Ming; and Chiang, Yun-Chih (2023) "Application of Unmanned Aerial Vehicle–Based Infrared Images in Determining Characteristics of Sea Surface Temperature Distribution," *Journal of Marine Science and Technology*: Vol. 31: Iss. 1, Article 2.
DOI: 10.51400/2709-6998.2681
Available at: https://jmstt.ntou.edu.tw/journal/vol31/iss1/2

Application of Unmanned Aerial Vehicle–Based Infrared Images in Determining Characteristics of Sea Surface Temperature Distribution

Acknowledgements

This research is partially supported by the “Integrated Environmental Quality Monitoring Plan for Hualien Hoping Industrial Zone during Operation” of Hoping Industrial Port Corporation and Ministry of Science and Technology, Taiwan, R.O.C. under Grant no. MOST 110-2221-E-320-004-.

RESEARCH ARTICLE

Application of Unmanned Aerial Vehicle−Based Infrared Images in Determining Characteristics of Sea Surface Temperature Distribution

Hsing-Yu Wang [a], Hui-Ming Fang [b], Yun-Chih Chiang [c,*]

[a] Department of Shipping Technology, College of Maritime, National Kaohsiung University of Science and Technology, Taiwan
[b] Bachelor Degree Program in Ocean Engineering and Technology, National Taiwan Ocean University, Taiwan
[c] Center for General Education, Tzu Chi University, Taiwan

Abstract

This study investigated the temperature field of a body of water by using rotary-wing unmanned aerial vehicles (DJI Mavic 2 Enterprise Dual) comprising visible light and infrared cameras to determine sea temperature distribution. With a flight height of 150 metres, image overlap of 80%, and image resolution of 4.75 cm/pixel, the proposed method was more effective than the conventional portable conductivity−temperature−depth device in rapidly measuring sea surface temperature and determining sea temperature distribution. The discharged heated water of the Hoping Power Plant traveled 100−330 metres from the wastewater outfall and then gradually diffused in the range of 100−490 metres before reaching a similar temperature to the background sea temperature. The diffusion of the thermal plume was mainly affected by regional marine meteorological conditions.

Keywords: UAV, Infrared camera, Temperature diffusion, Heated water discharge

1. Introduction

Water temperature is an indicator of the ecological environment. The diffusion of heated water discharge in waters surrounding wastewater outfalls is a major task in the hydrologic surveillance of power plants and a widely researched topic for scientists and engineers [1−6]. The cycle in which water is drawn in by a power plant as cooling water, discharged after being heated by generators, and then diffused into the sea is strongly affected by the currents, salinity, and tides of the marine environment in which this cycle takes place. The investigation of heated water discharge serves two purposes: to allow power plants to determine whether a rise in temperature in a body of water is within regulations and to provide scientific evidence to evaluate the effects of heated water discharge on adjacent bodies of water [7−10]. Generally, heated cooling water is discharged in the form of surface discharge through a outfall. After the heated water is discharged into the sea in the form of surface discharge, depending on its kinetic properties, the transportation and diffusion of the discharge can be assessed using a near-field or far-field model. A near-field model is primarily used in cases of a buoyancy effect occurring near a wastewater outfall, which is caused by the difference in density between the discharged heated water (driven by initial momentum) and the water in the environment as well as the convection effect between the discharged heated water and cold seawater. In the far-field model, because the movement of the discharged heated water is affected by the water in the environment, diffusion, and surface cooling, the heat from the discharged

---

Received 4 January 2022; revised 26 December 2022; accepted 30 December 2022.

* Corresponding author.
E-mail address: ycchiang@gms.tcu.edu.tw (Y.-C. Chiang).

https://doi.org/10.51400/2709-6998.2681

water dissipates primarily through convective flows. Therefore, this model mainly addresses convection and diffusion because the influence of initial momentum and the buoyancy effect decreases with distance. Because the diffusion of heated water can change the spatial distribution of bodies of water, observing the spatial distribution of bodies of water around wastewater outfalls is critical in the monitoring of nearshore ecology [11−13].

Sea temperature monitoring mainly involves the use of anchored buoys (Eulerian-type) to measure the temperature at fixed locations or portable conductivity−temperature−depth (CTD) devices to monitor water temperature diffusion [14−16]. Factors such as operational costs, procedural concerns, and time constraints can make the rapid monitoring of a specific area challenging. Temperature fields in the sea are mainly monitored using images and data from remote sensing satellites, which are corrected and verified using empirical formulas or simulations based on data measured in situ [17−22]. The limited scale of these images prevents satellite remote sensing from adequately reflecting local changes in a specific area. By contrast, aerial photogrammetry with unmanned aerial vehicles (UAVs) is a low-cost process and involves a low flight altitude, offering high operational efficiency and high mobility. This approach is highly developed; most UAVs currently in use are equipped with a global positioning system (GPS), an inertial measurement unit (IMU), and an autopilot mode, which simplifies control and effectively reduces operator errors. These features enable UAVs to capture high-precision images and record the locational information of these images, which greatly increases the credibility of the measurement data.

The problem of discharged heated water is related to energy transmission, which differs from that of other types of pollution (e.g., organic and inorganic compounds) [23−25]. To determine whether temperature changes caused by heated water discharged from a power plant affect the environment, the nearshore diffusion of discharged heated water and the associated rise in temperature must be monitored. Both governments and power plants are responsible for ensuring that discharged heated water complies with all relevant standards. Rule 7, No. 2, of the Water Pollution Control Act of the Environmental Protection Agency of Taiwan's Executive Yuan is the discharge standard, which states that discharge water must be directly discharged into the ocean and that the temperature of the discharge outlet shall not exceed 42 °C and be within 500 metres of the discharge outlet and the temperature difference of the surface water shall not exceed 4 °C. Infrared cameras are widely used in the field of temperature measurement because of their noncontact measurement method, wide temperature sensing range, measurement results that can be verified, low power consumption, portability, and other advantages. However, because of the influence of measurement distance on the accuracy of infrared cameras, their measurement accuracy does not meet high-precision requirements, thus limiting the scope of application of the instrument. The use of external configuration or analysis methods, such as those assessing related factors, can effectively reduce the effects of measurement distance on infrared camera accuracy, which can expand the scope of their application. The use of infrared cameras to measure heat transfer between convective flows has proved highly effective in measuring the surface thermal flux of a complex-shaped object in a flow field [23-28]. However, the water temperature distribution obtained through either satellite images or UAV infrared cameras only indicates the temperature distribution on the surface of the sea. Therefore, to understand the extent of the impact of cooling water discharge on the sea area, this study investigates the local temperature field of the water body. UAVs with onboard infrared cameras were used to measure the temperatures of an area in the sea, and the data were verified through comparison with data obtained in situ. Through this approach, we developed a method that rapidly generated data on a maritime temperature field, including the temperature distribution at the surface of the sea, the range of heated water diffusion, and temperature changes.

2. Materials and methods

2.1. UAV photogrammetry

UAV photogrammetry, a type of aerial survey technology, is a remote sensing technique in which instrument-carrying UAVs capture a series of images of a target from the air. The instrument can be a camera, video camera, or sensor, and the images provide information regarding the shape, location, or other attributes of a target for additional applications. Aerial triangulation principles are applied in the aerial survey. First, tie points (or pass points) appearing in a series of images of an area are measured. Then, a spatial coordinate system based on data collected in situ from control points on the ground is added to convert the data in the aerial images into numerous three-dimensional coordinates for further analysis. A collinearity equation forms the basis of aerial survey. By assuming a straight line (O-a-A) between a target in the coordinate system of the object space (the real world), the image of the target in the coordinate system of the image space, and the center of the photograph (camera's perspective center) in the coordinate system of the object (Fig. 1), the relationship between the coordinate system of the image space and that of the object space can be established, as in (1).

$$x_a - x_0 = -f\frac{m_{11}(X_A - X_L) + m_{12}(Y_A - Y_L) + m_{13}(Z_A - Z_L)}{m_{31}(X_A - X_L) + m_{32}(Y_A - Y_L) + m_{33}(Z_A - Z_L)}$$

$$y_a - y_0 = -f\frac{m_{21}(X_A - X_L) + m_{22}(Y_A - Y_L) + m_{23}(Z_A - Z_L)}{m_{31}(X_A - X_L) + m_{32}(Y_A - Y_L) + m_{33}(Z_A - Z_L)} \quad (1)$$

In (1), x_a and y_a are the coordinates of image point a in the coordinate system of the image space; x_0 and y_0 are the coordinates of the principal point (PP) in the fiducial coordinate system, which represent the displacement of the PP relative to the fiducial center; f is the focal length of the camera, which is also the principal distance of the image; X_A, Y_A, Z_A are the target's coordinates in the coordinate system of the object space; X_L, Y_L, Z_L are the coordinates of the camera's perspective center in the coordinate system of the object space; and $m_{11} - m_{33}$ are elements that constitute rotation matrix m and consist of the UAV's rotation (attitude) parameters, as shown in (2).

$$m = \begin{bmatrix} m_{11} & m_{12} & m_{13} \\ m_{21} & m_{22} & m_{23} \\ m_{31} & m_{23} & m_{33} \end{bmatrix} = \begin{bmatrix} \cos\varphi\cos\kappa & \cos\omega\sin\kappa + \sin\omega\sin\varphi\cos\kappa & \sin\omega\sin\kappa - \cos\omega\sin\varphi\cos\kappa \\ -\cos\varphi\cos\kappa & \cos\omega\cos\kappa - \sin\omega\sin\varphi\sin\kappa & \sin\omega\cos\kappa + \cos\omega\sin\varphi\sin\kappa \\ \sin\varphi & -\sin\omega\cos\varphi & \cos\omega\cos\varphi \end{bmatrix} \quad (2)$$

Because the target point, the corresponding point in the image, and the center of the image (the camera's perspective center) must form a straight line, the light beam method can be applied for aerial triangulation. In this method, each image is used as a basic adjustment calculation unit; each photo taken by the camera constitutes a light beam, and the intersections of two or more light beams are used to connect multiple images into an area for adjustment calculation. In bundle adjustment using the light beam method, interior orientation parameters, exterior orientation parameters, and lens distortion are substituted into the aerial triangulation equation as constants. Therefore, when self-calibration bundle adjustment (“bundle adjustment with added parameters”) is performed, interior orientation parameters, exterior orientation parameters, and lens distortion should be considered unknown values and calculated accordingly to improve the accuracy of the adjustment results.

Interior orientation parameters refer to the relative positions of the camera's perspective center and the image plane within the camera. The interior orientation parameters of the typical nonmetric cameras on UAVs are usually unknown or less stable than those of metric cameras specially designed for photogrammetric purposes. Therefore, they should be calculated and calibrated to help correct the offset in images. The flight path (including latitude, longitude, and flight height) recorded by GPS systems, which are installed on most UAVs, can serve as a reference for the interior orientation parameters. Six exterior orientation parameters are used: spatial coordinates X, Y, Z and rotation angles (attitude parameters) ω, φ, κ. These parameters describe a UAV's position (i.e., the camera's perspective center) and the attitude, which indicate the location and angle from which an image is captured. Direct georeferencing technology can be integrated with three-dimensional coordinates (provided by onboard GPS) and angular deflection and acceleration values on three axes (measured by onboard IMU) to accurately calibrate a UAV's position, flight path, and attitude, thereby making exterior orientation parameters directly available and greatly reducing the time and workload required for image generation through conventional aerial photogrammetry.

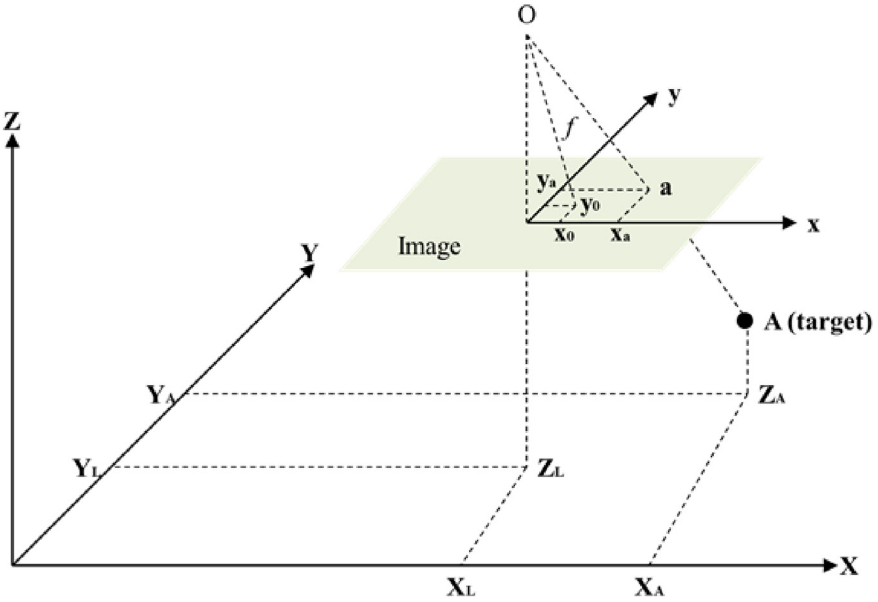

Fig. 1. Diagram of the collinearity equation (modified from that presented in [26]).

2.2. Image calibration

Out of mobility and economic considerations, the DJI Mavic 2 Enterprise Dual rotary-wing drone was selected (Fig. 2). Table 1 presents its specifications. The drone carries a visible light camera and an infrared camera, is light and portable, and can be folded and stored in a box. It has a maximum flight time of 31 minutes and a maximum signal transmission range of 8 km. It can reach an elevation of 6000 metres and is equipped with an omnidirectional sensor, an intelligent obstacle avoidance module, and an advanced pilot assistance system, which enables it to automatically plan its flight path. However, because it uses a nonmetric camera, image calibration must be performed in advance to obtain the interior orientation parameters. We used the method proposed in [2,29], and a 30 × 24 cm^2 aluminum board consisting of 6 × 6 cm^2 grids in a checkered pattern heated by a lamp was used as the calibration target (Fig. 3). After the aluminum board was heated by a lamp placed behind it, its covered and uncovered parts appeared as a checkerboard through the infrared camera, making the calibration points clearly discernable. Then, the DJI Mavic 2 Enterprise Dual drone was used to capture images of the aluminum board from various angles with the onboard infrared thermal camera. The images were then imported to an image calibration program for further calibration. Figs. 4–6 present the results.

Fig. 2. DJI Mavic 2 Enterprise Dual drone.

2.3. Photogrammetry flight planning

In the design of a flight route, battery life and imagery overlap must be considered. The application of aerial surveying to overlapping areas is mainly for better image matching and combination. For the end lap, to achieve better image matching and combination results for adjacent images on the route, the recommended imagery overlap rate is 80%. For the side lap, to prevent line spacing from being affected by flight deviation angles, altitude changes, or terrain changes, the recommended imagery overlap rate is more than 30%, which prevents image combination errors. An end lap of 80% and a side lap of 30% or more are recommended to achieve a favorable three-dimensional image match and image mosaic results. Fig. 7(a) and (3) and present the concept and formula for the end lap, respectively. In (3), B represents the distance from

Table 1. Specifications of DJI Mavic 2 Enterprise Dual drone and its onboard infrared thermal camera.

Take-off weight (max.) 1100 g	**Lens** Angle of view: 57°(HFOV) Aperture: $f/1.1$	**Dimensions (L × W × H)** Folded: 214 × 91 × 84 mm Unfolded: 322 × 242 × 84 mm
Resolution 160*120	**Diagonal length** 354 mm	**Pixel pitch** 12 μm
Detectable wavelength 8-14 μm	**Descending speed (max.)** 3 m/s	**Image size** 640 × 480 (4:3); 640 × 360 (16:9)
Climb rate (max.) 5 m/s (S mode); 4 m/s (P mode)	**Speed in level flight (max.)** [a] 72 km/h (S mode); 50 km/h (P mode)	**Camera modes** Single shot; Burst: 3/5/7 shots; Time lapse: 2/3/5/7/10/15/20/30/60 s
Flight elevation (max.) 6000 m	**Image resolution** 640*360@8.7fps	**Flight time (max.)** [b] 31 min
Precision in temperature sensing [c] High gain mode: 5% maximum Low gain mode: 10% maximum	**Wind speed (max.)** Beaufort force 5	**Dynamic range** High gain mode: −10–140 °C Low gain mode: −10–400 °C
GNSS GPS + GLONASS	**Image format** JPEG	**Video format** MP4 MOV(MPEG-4 AVC/H.264)

[a] Measured at sea level under windless conditions.
[b] Under windless conditions and a constant speed of 25 km/h.
[c] Typical values.

the center of one image to that of the next (i.e., the air base), and G represents the length on the ground covered by each image. The overlapping area covered by two consecutive images is the end lap. Fig. 7(b) and (4) present the concept and formula for the side lap, respectively. The two flight routes have an interval of W ("flight line spacing"), and each image covers the length G. The overlapping area covered by the two consecutive images is the side lap.

$$PE=\left(\frac{G-B}{G}\right)\times 100(\%) \tag{3}$$

$$PS=\left(\frac{G-W}{G}\right)\times 100(\%) \tag{4}$$

Fig. 3. Calibration target consisting of an aluminum board in a checkered pattern and a lamp.

In (3) and (4), PE and PS denote end lap and side lap (unit: %), respectively; G represents the length covered by one image; B represents the air base; and W represents the flight line spacing. In addition to image overlap, the relationship between ground sample distance (GSD) and flight height must be considered. As shown in Fig. 8, light beams reflected by objects on the ground travel the distance of the flight height (AGL), pass through the lens, and continue to travel the distance of the focal length to form an image on the imaging component of the camera. Therefore, the ratio of GSD to ground horizontal distance and the ratio of GSD to flight height must be calculated according to the resolution of the imaging component, as shown in (5).

$$\frac{Pixel\ Size}{Focal\ Length}=\frac{GSD}{AGL} \tag{5}$$

The number of images, image overlap, and camera range can be used to estimate total flight time (excluding the time for take-off and the return trip), which can then be used to estimate operational requirements.

3. Results and discussion

3.1. Overview of the experimental site

To verify the accuracy of the infrared sea temperature measurements, we selected a site that allowed the simultaneous collection of marine meteorological data, including temperature, wind force, and current. The information published by Taiwan's Environmental Protection Agency was

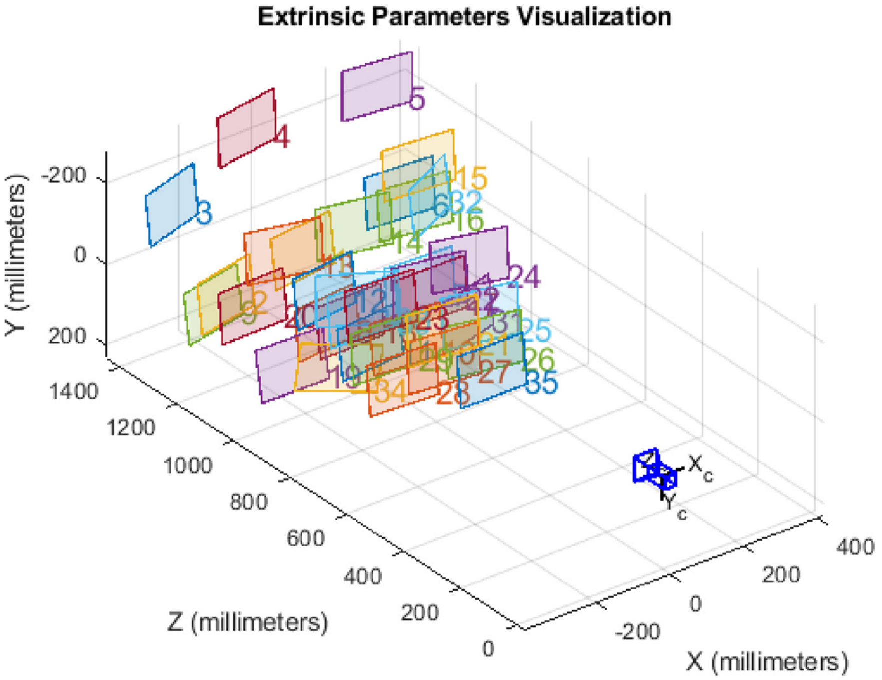

Fig. 4. Relative position of the camera in spatial coordinate system.

referenced, and a suitable site was identified near Hoping, Hualien. The Hoping Power Plant draws seawater from Hoping harbor, transfers heat unable to be converted into electricity to the water, and then discharges the water back into the sea after it has been heated. This creates thermal plumes and water temperature diffusion in the waters around the plant, making the region ideal for this study. The area within 500 m of the plant's wastewater outfall was marked as the experimental site (the red line in

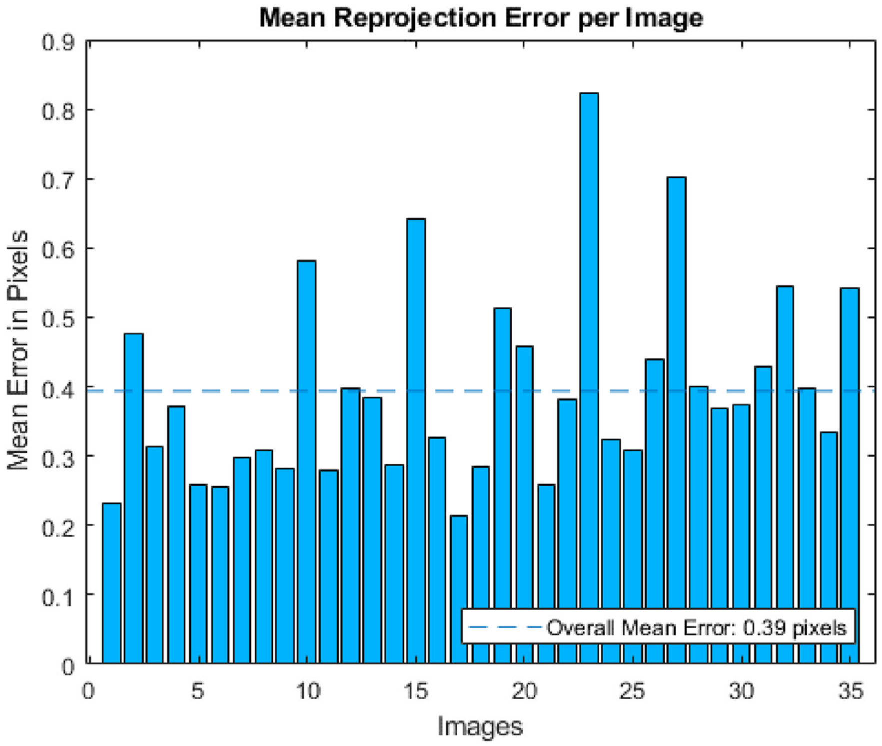

Fig. 5. Mean reprojection error per image (0.39 pixels).

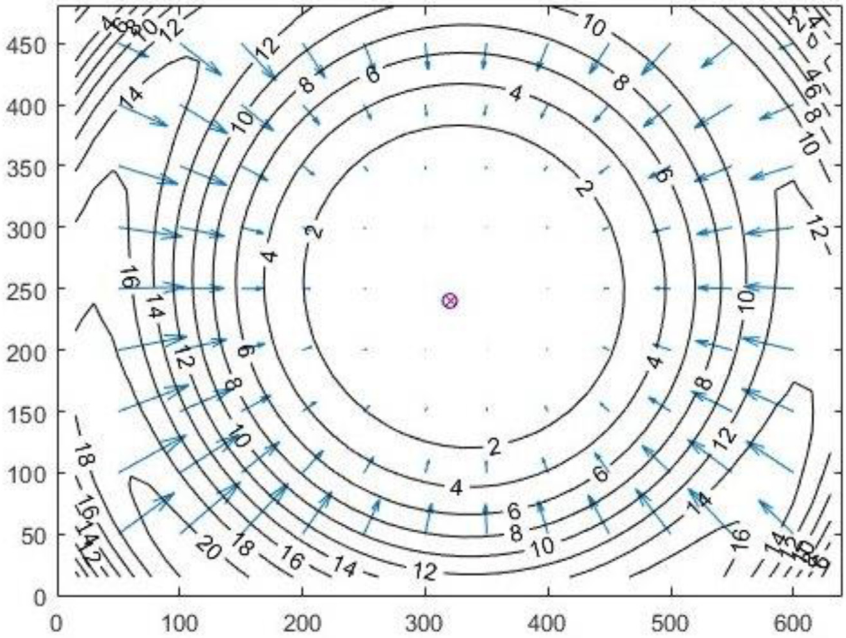

Fig. 6. Mean pixel shift after calibration.

Fig. 9), and the research team collected data and conducted in situ measurements to verify the ability of the proposed temperature measurement method to accurately present surface layer temperature distribution and diffusion. To satisfy the photogrammetric requirements and maintain the power consumption level of the UAV at one battery per one-way trip, the single S mode was selected as the route mode, with the end lap and side lap both set at 80% (Table 2 and Fig. 10).

3.2. Thermal imager temperature calibration

The longitude and latitude readings recorded by the UAV's compass and those of the images' centers were used to translate the images to corresponding longitudes and latitudes for image synthesis. Throughout the image synthesis process, the thermal imaging results were unified to set a temperature threshold, and then, a grayscale comparison was performed. After setting the upper and lower temperature limits for the thermal imaging result, we set the grid cell of the image synthesis to obtain the temperature distribution results of the whole range. Image synthesis application could then be carried out. Fig. 11 presents the image synthesis application results, which were overlaid onto a Google Earth map of the coastline shown in the image. The temperature distributions in the area were then analyzed.

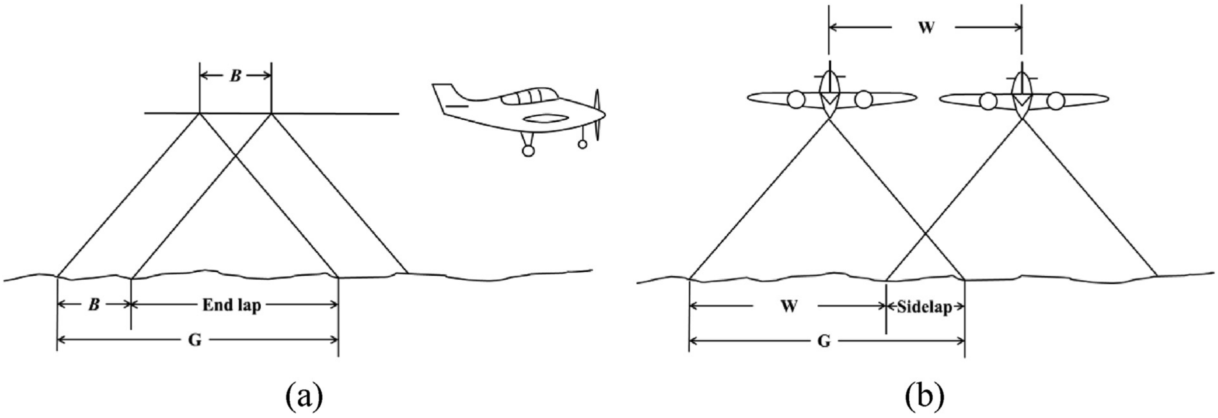

Fig. 7. End lap and side lap.

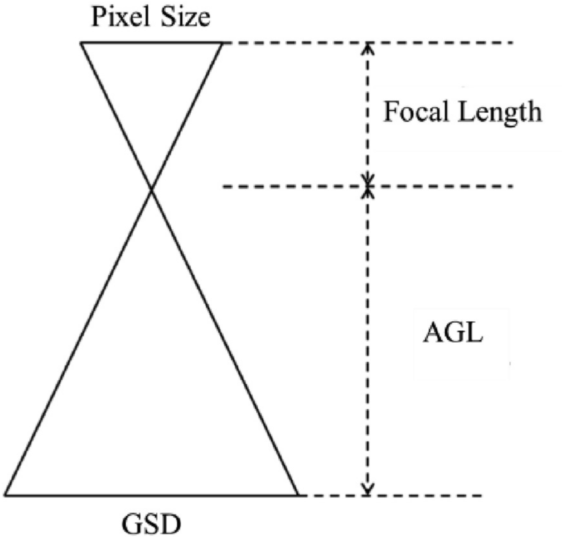

Fig. 8. Relationship between ground sample distance and flight height.

To determine the accuracy of the infrared sea temperature measurements, a test flight was performed from 21:00, October 13, to 18:00, October 14, 2019, and the measurements taken during the test flight were compared with those published in the Biological Survey of Waters Near Hoping Power Plant for calibration. The report did not contain readings for the area 500 m from the waste water outfall because the instruments at Stations T1 (121.77470°, 24.31065°) and T3 (121.76903°, 24.30062°), which were deployed 500 m from the outfall, were missing. Consequently, the readings from Station T2 (121.77297°, 24.30574°), which was deployed 250 m from the outfall, were used as the control data. Because regional meteorological conditions can cause the properties of discharged heated water to vary at different times of day, we referenced the tidal prediction chart of the Central Weather Bureau and took infrared images at high tide, slack tide, and low tide. Fig. 12 presents the results of the comparison; the blue line represents the water temperature measured in situ, the red line represents the infrared temperature measurements, and the green line represents the difference between the two. The results indicate that the infrared readings were lower than those measured in situ by approximately 2.4 °C. This difference can be attributed to the high humidity at the experimental site, which caused absorption of the infrared radiation, causing the discrepancy.

3.3. Experimental results and discussion

This study used UAVs with infrared cameras to measure sea temperature and identified the temperature distribution at the surface of the sea, the range of heated water diffusion, and temperature changes. The parameters were calibrated on October 14, 2019, and the UAV-based infrared images of the surface seawater were taken between 19:00, February 19, and 14:00, February 21, 2020. Fig. 13 presents the resulting images taken during 12 time periods. The timing of this experiment coincided with an instrument deployment operation by the Biological Survey of Waters Near Hoping Power Plant (beginning at 12:00, February 20, 2020). Therefore, the results of this experiment are presented together with data on sea currents to

Fig. 9. Experimental site near Hoping, Hualien.

Table 2. UAV flight plan.

Flight height	Flight time	Number of images	End lap and side lap	Image resolution
150 m	10′12″	109 p	80%	4.75 cm/pixel

determine the effect of the surface flow field in addition to the range of heated water diffusion.

The land and sea are clearly demarcated in the images because the temperature of the land was heavily affected by sunlight. The image from 19:46, February 19, 2020, was taken during a northeasterly wind of 2.27 m/s, and the thermal plume moved south along the shore for some distance before turning to the northeast; its jet reached as far as 330 m south of the wastewater outfall. Diffusion began at 140 m southeast of the wastewater outfall. The thermal plume was affected by the wind at this point and began to diffuse toward the northeast. The image from 22:26, February 19, 2020, was taken during a northwesterly wind of 5.25 m/s, when the sea was warm. The thermal plume moved south covering some distance before beginning to diffuse toward the northeast. The jet of the thermal plume reached 160 m southeast of the wastewater outfall. The image from 02:01, February 20, 2020, was taken during a northwesterly wind of 2.51 m/s. The thermal plume moved southeast before turning northeast and beginning to diffuse under the influence of the wind. The jet of the thermal plume reached 140 m southeast of the wastewater outfall. The image from 05:01, February 20, 2020, was taken during a northwesterly wind of 0.71 m/s, and the sea surface exhibited a high mean temperature during this time. The jet of the thermal plume reached 140 m southeast of the wastewater outfall before turning northeast and beginning to diffuse. However, the range of diffusion was not clear, and by the time the thermal plume reached 100 m northeast of the tip of the jet, its temperature was approaching the background value. The image from 07:50, February 20, 2020, was taken during a northwesterly wind of 3.5 m/s, and the effect of sunlight was highly pronounced at this time. The temperature of the land was increasing, and although the temperature at sea (the background value) was high, the jet of the thermal plume and its direction and distance of diffusion were discernable; it reached 150 m southeast of the wastewater outfall before beginning to diffuse toward the northeast under the influence of the growing wind. The image from 10:00, February 20, 2020, was taken during a northerly wind of 0.74 m/s, and the temperature of the land during this time was extremely high. Because the wind had subsided, the diffusion began more quickly than it had previously; the jet of the thermal plume began to diffuse toward the northeast at 130 m southeast of the wastewater outfall.

The proceeding results were generated by considering the effect of the sea currents. The image from 17:30, February 20, 2020, was taken during a northwesterly wind of 2.89 m/s, which shows that and the thermal plume moved 240 m southeast before beginning to diffuse toward the northeast. The sea current observed in situ at that time moved toward the northwest at a flow rate of 0.1 m/s on the surface. The image is consistent with the in situ observation in that the flow mainly went from the northwest of the tip of the jet toward the northeast. In the image taken at 19:30, February 20, 2020, the wind turned west by west–northwest and decreased to 0.82 m/s, the jet of the thermal plume reached

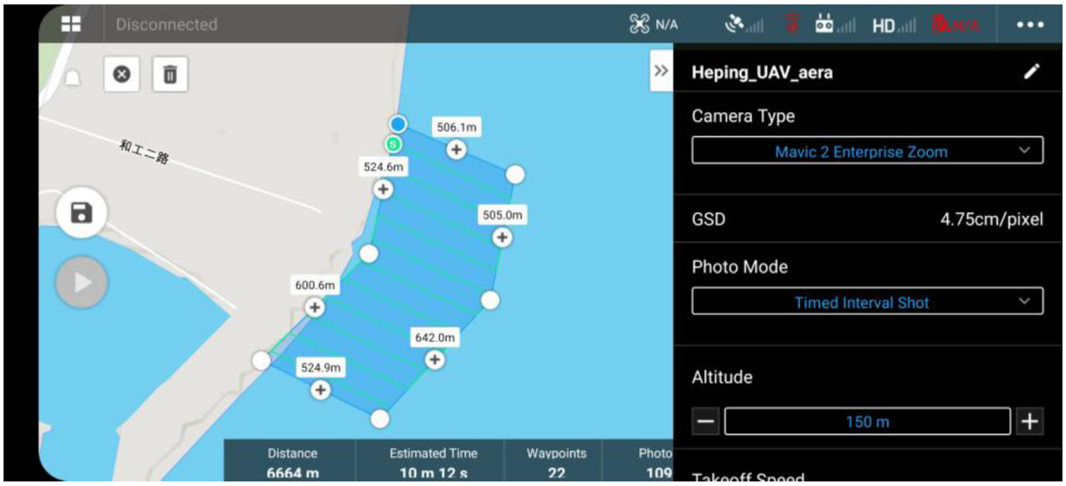

Heping_UAV_aera

Camera Type: Mavic 2 Enterprise Zoom

GSD: 4.75cm/pixel

Photo Mode: Timed Interval Shot

Altitude: 150 m

Takeoff Speed

Distance	Estimated Time	Waypoints	Photo
6664 m	10 m 12 s	22	109

Fig. 10. Planned flight route.

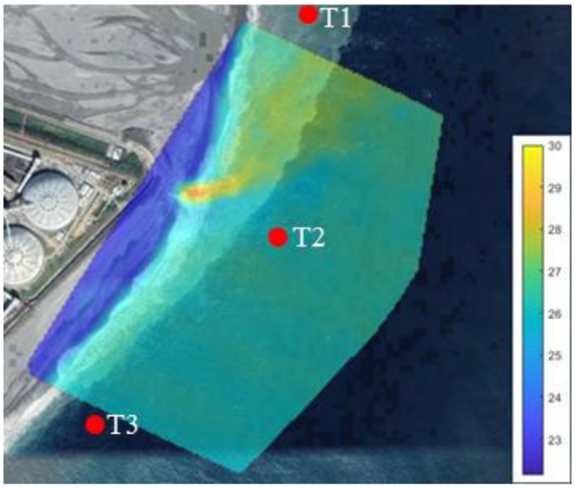

Fig. 11. Synthesized infrared image of experimental site.

approximately 180 m southeast of the wastewater outfall, and diffusion occurred mainly toward the northeast. The sea current observed in situ moved toward the northeast at a flow rate of 0.27 m/s on the surface. The image is consistent with in situ observations despite the weak flow rate. The image from 23:00, February 20, 2020, was taken during a northwesterly wind of 2.82 m/s, and the jet of the thermal plume reached approximately 220 m southeast of the wastewater outfall before beginning to diffuse toward the northeast. The sea current observed in situ moved toward the northeast at a weak flow rate of 0.08 m/s on the surface. The image indicates that the range of diffusion was small. The image from 02:36, February 20, 2021, was taken during a northwesterly wind of 1.05 m/s, and the tip of the jet of the thermal plume reached 140 m east of the wastewater outfall. The sea current observed in situ moved toward the northeast at a high flow rate of 0.60 m/s on the surface. The image is consistent with in situ observations in that the direction of diffusion matched that of the observed flow direction, and the larger diffusion distance reflected the higher flow rate. In the image taken at 10:50, February 20, 2021, the wind turned northeast and the speed increased to 2.89 m/s, and the tip of the jet of the thermal plume reached 100 m east of the wastewater outfall. The sea current observed in situ moved toward the north at a slightly low flow rate of 0.45 m/s on the surface. The image is consistent with in situ observations in that the direction of the flow matched that of the diffusion, but the range of diffusion did not differ from that of the previous one noticeably. The image from 13:50, February 20, 2021, was taken during a northeasterly wind of 4.75 m/s, and the tip of the jet of the thermal plume reached 110 m east of the wastewater outfall. The sea current observed in situ moved toward the northeast at a weak flow rate of 0.14 m/s on the surface. The image is consistent with in situ observations in that the direction of the flow matched that of the diffusion, but the range of diffusion was shorter than before.

The jet of the thermal plume observed through infrared imaging traveled 100–330 m, the direction of the thermal plume approximately matched that of the wind and the sea current, and the mean distance from the thermal plume to the comparable background sea temperature was 100–490 m. The infrared images were compared with the sea temperature at 1 m underwater reported by the Biological Survey for the Waters Near Hoping Power Plant, which was measured on February 21, 2020, by using a portable CTD (Fig. 14). The comparison revealed that the thermal plume diffused primarily toward the southeast and partially toward the northeast. The range of southeastward diffusion was within 500 m of the wastewater outfall. Furthermore, the results from the infrared images captured using the UAVs were consistent with the in situ measurements, which indicates that UAV-based photogrammetry is an effective strategy for the investigation of sea surface temperature distribution.

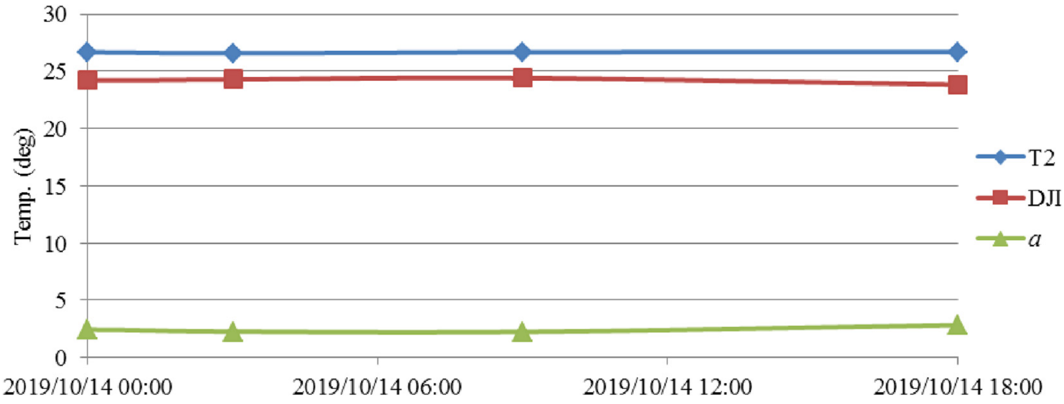

Fig. 12. Comparison of temperature readings.

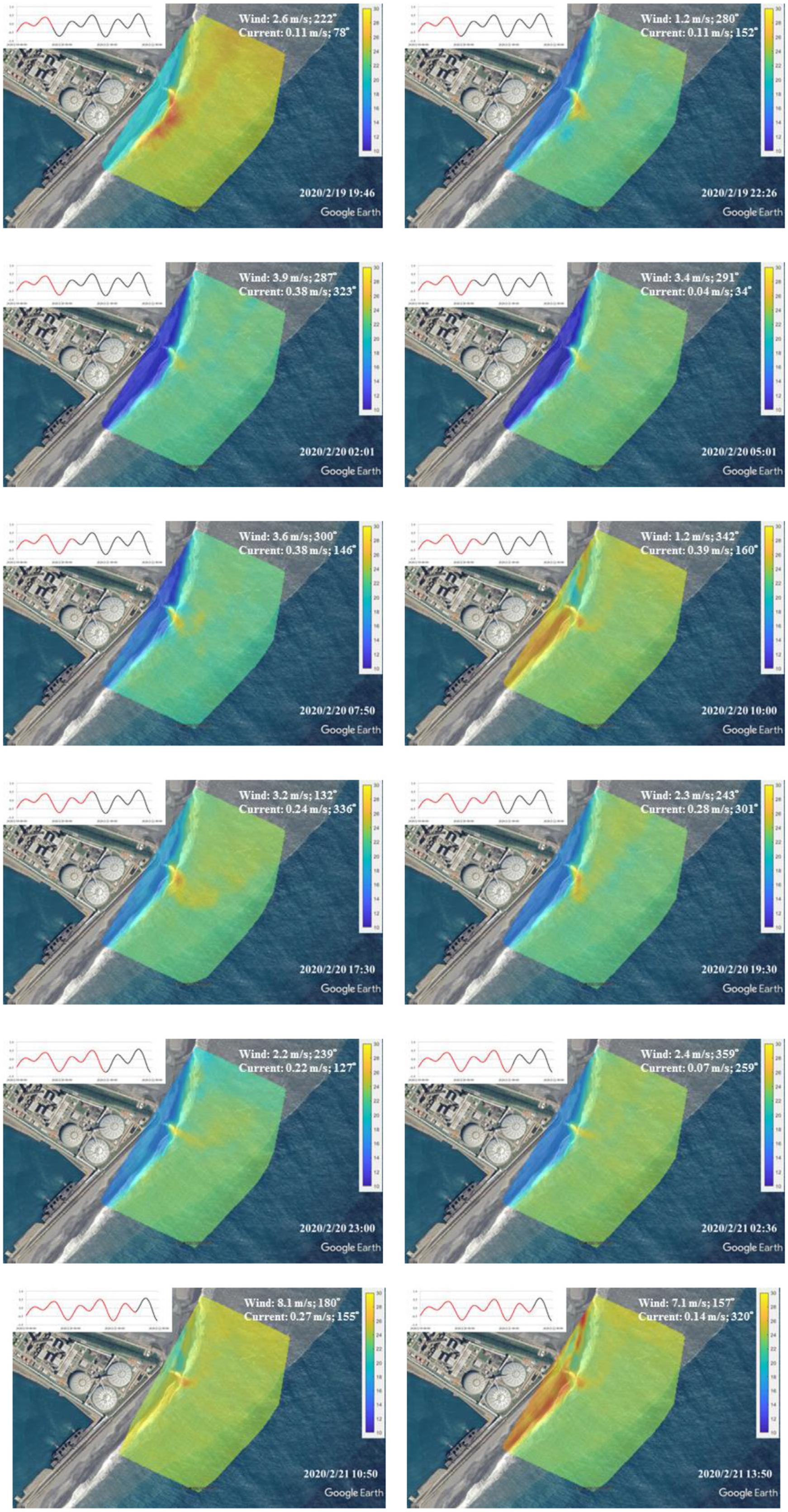

Fig. 13. Results from the unmanned aerial vehicle–based infrared camera.

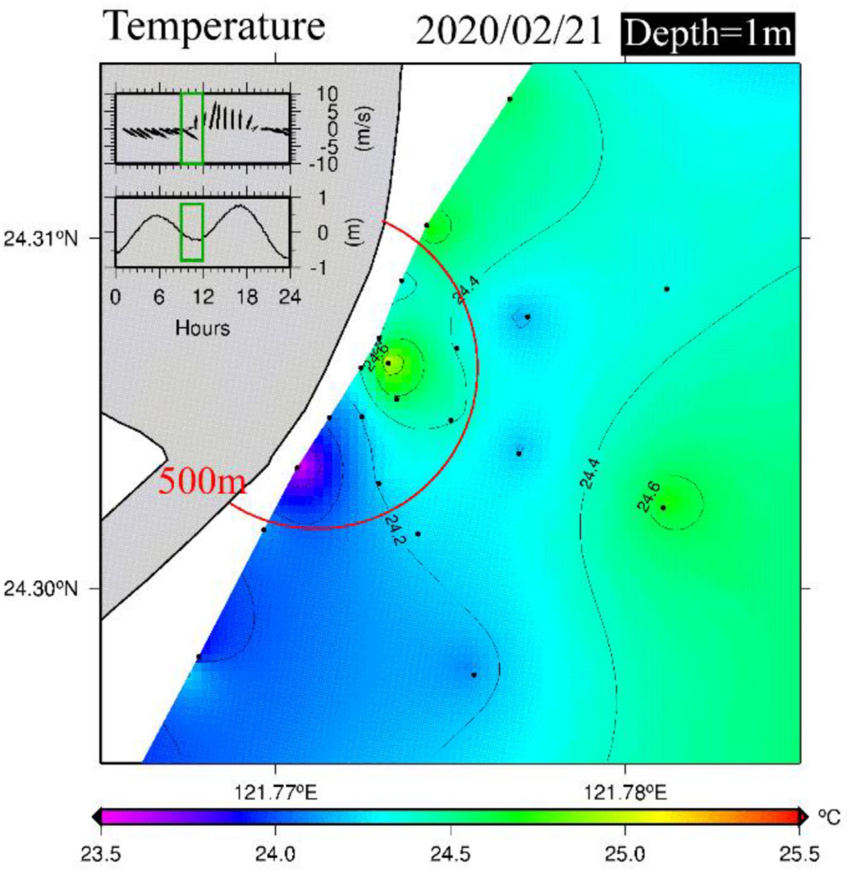

Fig. 14. Sea temperature at 1 m underwater. Source: Biological Survey of Waters Near Hoping Power Plant.

4. Conclusion

This study used rotary-wing UAVs carrying dual cameras to capture infrared images of an area 500 m in diameter for 12 min with a flight height of 150 m, an image overlap of 80%, and an image resolution of 4.75 cm/pixel. Compared with the conventional method, which involves measuring sea temperature at selected points, the method proposed by this study allows rapid measurement of the surface temperature of a nearshore area, determination of its temperature distribution, and monitoring of its temperature diffusion. The results indicate that the discharged heated water traveled 100−330 m from the wastewater outfall and gradually diffused at a range of 100−490 m until reaching a temperature close to the background sea temperature. Infrared images were captured consecutively for 24 hours to determine the natural environment's effect on the diffusion of discharged heated water, and the results suggest that infrared images taken in the early morning or between dusk and night yield better results than those taken at noon. This is primarily because sunlight causes reflection off the surface of the water, which produces noise in infrared images that affects data analysis. Generally, the diffusion of thermal plumes is affected by regional marine meteorological conditions. This study proposed a novel approach to observing sea temperature diffusion. However, the frequency of observation was not sufficient to accurately reflect the characteristics of sea temperature distribution. Future studies can increase the frequency of observation and apply statistical methods in comparison with data measured in situ to obtain more accurate data. In addition, numerical models can be used in such comparisons for more comprehensive research.

Conflict of interest statement

This research does not have any conflict of interest.

References

[1] Coles SL. Coloniza of Hawaiian reef corals on new and denuded substrata in the vicinity of a Hawaiian power station. Coral Reefs 1980;3:123−30.
[2] Martinez-Arroyo A, Abundes S, Gonzalez ME, Rosas I. On the Influence of Hot-Water Discharges on Phytoplankton

Communities from a Coastal Zone of the Gulf of Mexico. Water Air Soil Pol 2000;119:209–30.
[3] Melton BR, Serviss GM. Florida Power Corporation-Anclote Power Plant Entrainment Survival of Zooplankton. Environ Sci Pol 2000;3(S1):233–48.
[4] Leandro SM, Morgado F, Pereira F, Queiroga H. Temporal changes of abundance, biomass and production of copepod community in a shallow temperate estuary (Ria de Aveiro, Portugal), Estuarine. Coast Shelf Sci 2007;74:215–22.
[5] Niehoff B. Life history strategies in zooplankton communities: The significance of female gonad morphology and maturation types for the reproductive biology of marine calanoid copepods. Prog Oceanogr 2007;74:1–47.
[6] Teixeira TP, Neves LM, Araujo FG. Effects of a nuclear power plant thermal discharge on habitat complexity and fish community structure in Ilha Grande Bay, Brazil. Mar Environ Res 2009;68:188–95.
[7] Harleman DRF, Hall LC. Thermal diffusion of condenser water in a river during steady and unsteady flows with application to the TVA Browns Ferry nuclear plant. Hydrodyn Lab Rep 1968;3:98–115.
[8] David AL, Jorg I. Characteristics of a Surface Buoyant Jet. J Geophys Res 1987;92(C5):5435–47.
[9] Yanagi T, Sugimatsu K, Shibaki H, Shin HR, Kim HS. Effect of tidal flat on the thermal effluent dispersion from a power plant. J Geophys Res 2005;110:C03025.
[10] Huang F, Lin J, Zheng B. Effects of Thermal Discharge from Coastal Nuclear Power Plants and Thermal Power Plants on the Thermocline Characteristics in Sea Areas with Different Tidal Dynamics. Water 2019;11:2577. https://doi.org/10.3390/w11122577.
[11] McGuirk JJ, Rodi W. A depth averaged mathematical model for near field of side Discharges into open channel flow. J Fluid Mech 1978;86:761–81.
[12] Hamrick JM, Mills WB. Analysis of water temperatures in Conowingo Pond as influenced by the Peach Bottom atomic power plant thermal discharge. Environ Sci Pol 2000;3:197–209.
[13] Poornima EH, Rajadurai M, Rao TS, Aunpkumar B, Narasimhan SV, Rao VNR, Venugopalan VP. Impact of thermal discharge from a tropical coastal power plant on phytoplankton. J Water Res 2005;30:307–16.
[14] Leigh Bridges W, Anderson R D. A brief survey of Pilgrim Nuclear Power Plant effects upon the marine aquatic environment. Observations on the Ecology and Biology of Western Cape Cod Bay, Massachusetts, 1984;11:263–71.
[15] Sündermann J. Survey: Sources, paths and effects of marine pollution. In: Pollution of the Sea — Prevention and Compensation. Berlin, Heidelberg: Springer; 2007. p. 7–14.
[16] Lee JH, Ro YJ, Cho YK. A Standard Guide to Physical Oceanographic Survey of the Effect of Thermal Discharge from a Nuclear Power Plant. Sea: J Kor Soc Oceanogr 2007; 12:43–9 (in Korea).
[17] Lathrop RG, Lillesand TM. Use of Thematic Mapper Data to Assess Water Quality in Green Bay and Central Lake Michigan. Photogramm Eng Rem Sens 1986;52(5): 671–80.
[18] Gibbons DE, Wukelic GE. Application of Landsat Thematic Mapper Data for Coastal Thermal Plume Analysis at Diablo Canyon. Photogramm Eng Rem Sens (USA) 1989; 55(6):903–9.
[19] Arbelo M, Herrera F, Exposito FJ, Caselles V, Coll C. Determination of Sea Surface Temperature Using Combined TOVS and AVHRR Data. Application to the Canary Islands area, Spain. Int J Rem Sens 1996;17(2):359–71.
[20] Mustard J, Carney M, Sen A. The Use of Satellite Data to Quantify Thermal Effluent Impacts, Estuarine. Coast Shelf Sci 1999;49:509–24.
[21] Emery WJ, Castro Sandra, Wick GA, Peter Schluessel, Craig Donlon. Estimating Sea Surface Temperature from Infrared Satellite and In Situ Temperature Data. Bull Am Meteorol Soc 2001;82(12):2773–85.
[22] Ahn YH, Shanmugam P, Lee JH, Kang YQ. Application of satellite infrared data for mapping of thermal plume contamination in coastal ecosystem of Korea. Mar Environ Res 2006;61:186–201.
[23] Chrzanowski K. Problem of determination of effective emissivity of some materials in MIR range. Infrared Phys Technol 1995;36:679–84.
[24] Chrzanowski K. Influence of object-system distance on accuracy of remote temperature measurement with IR systems. Infrared Phys Technol 1995;36:703–13.
[25] Astarita T, Cardone G, Carlomagno GM, Meola C. A survey on infrared thermography for convective heat transfer measurements. Opt Laser Technol 2000;32:593–610.
[26] Krapels KA, Driggers RG, Vollmerhausen RH, Kopeika NS, Halford CE. Atmospheric turbulence modulation transfer function for infrared target acquisition modeling. Opt Eng 2001;40(9):1906–13.
[27] Kargel C. Infrared thermal imaging to measure local temperature rises caused by handheld mobile phones. IEEE Trans Instrum Meas 2005;54:1513–9.
[28] Kylili A, Fokaides PA, Christou P, Kalogirou SA. Infrared thermography (IRT) applications for building diagnostics: A review. Appl Energy 2014;134:531–49.
[29] Zhang Z. A flexible new technique for camera calibration. IEEE Trans Pattern Anal Mach Intell 2000;22(11):1330–4.